

# Double symmetry and phase-controlled continuous transformation between skyrmion and meron topology

SEN LU,<sup>1,2</sup> XIONGXIONG,<sup>1</sup> XUEFEI ZI,<sup>1</sup> AND ZHE SHEN<sup>1,\*</sup>

<sup>1</sup>*School of Electronic and Optical Engineering, Nanjing University of Science and Technology, Nanjing 210094, China*

<sup>2</sup>*lusen@njust.edu.cn*

*\*shenzhe@njust.edu.cn*

**Abstract:** Topological quasiparticles, including skyrmions and merons, are topological textures with sophisticated vectorial structures that can be used for optical information storage, precision metrology, position sensing, etc. Here, we build a simple model to generate the isolated Néel-type field-skyrmion and derive the analytical solution of it. By employing a series of well-designed double-symmetry apertures and controlling the initial phase of light, we realized the continuous transformation between the isolated skyrmion, the meron lattice, and the skyrmion lattice. We show that the field symmetry determines the possible forms of the topological texture, and the initial phase switches the presentation form of it. These results enrich the methods for generating and transforming topological textures, provide new insights into the symmetry of the electromagnetic field, and open up new opportunities for precision measurement and topological photonics.

## 1. Introduction

In 1962, the British physicist Tony Skyrme found a kind of quasiparticle with topological protection by solving nonlinear field theory equations, namely skyrmion [1]. Possessing a topological non-trivial spin texture, it is the product of the combination of topology and condensed matter, demonstrated in liquid crystals [2], Bose-Einstein condensates [3], chiral magnets [4], and so on. Similar to skyrmions, merons, also known as half-skyrmions, are topological quasiparticles with half-integer topological charges, which have been reported in the form of a lattice [5, 6]. In past decades, magnetic skyrmions, due to their small size, low current drive, and topological stability [7], have created amazing achievements in high-density data storage [8, 9], logic gates [10, 11], and other spintronic devices. As the counterpart of magnetic skyrmions, optical skyrmions have recently attracted much interest for their sophisticated spin texture and significant application potential [12-14].

The optical skyrmions were first observed in the evanescent electric field of surface plasmon polaritons (SPPs) generated on the hexagonal metal grating structure [15]. Following this configuration, the spin-orbit interaction of light in plasmonic lattices [16] has been studied. Afterward, Davis et al. realized the ultrafast vector imaging of plasmonic skyrmion, experimentally observing the dynamical skyrmion vector information [17]. Furthermore, the unique polarization properties [18], the dynamic control for the position and shape [19], and the localized magnetic plasmon skyrmions [20] appeared one after another. These excellent studies unveiled the fascinating properties of skyrmions and enriched the light-matter interactions at the sub-wavelength scale, however, these plasmonic-based models strongly depend on the hexagonal metal grating structure or multiple beams from different directions, which are complex, undoubtedly increasing the complexity and cost of the optical system. In addition, a fixed structure can only support one topological texture, which makes it difficult to study the relationships between different topologies.

Excepting the field skyrmion, the photonic skyrmion [21] based on the spin angular momentum also attracted much attention and provided deep insights into the generation and manipulation of the skyrmion family. For example, the symmetry controlled photonic spin

skyrmions and spin-meron lattice [22], the chirality related Bloch-type skyrmion and meron lattice [23, 24], and the phase dependent dynamic position control of photonic skyrmion [25]. Although great efforts have been made in the generation and manipulation of topological textures, however, the continuous transformation between skyrmion and meron topology has not yet been achieved, the mechanism of transformation is still blank, which is important in topological photonics and significant in revealing the evolution between different topological textures.

In this research, we utilize a simple three-layer model generated a Néel-type field skyrmion on the metal-air interface with a tightly focused circularly polarized vortex beam. We derived the analytical solution of it. Benefiting from the structureless excitation of skyrmions in a dynamic configuration, this method is convenient and does not depend on the complex hexagonal metal grating structure. Then, we place a square and hexagonal aperture behind the tightly focused beam and control the initial phase of it, realizing the transformation from the isolated skyrmion to the meron lattice and the skyrmion lattice, respectively. We show that both the square and hexagonal apertures have double-symmetry properties, i.e., circular symmetry in the center and fourfold or sixfold symmetry near the corners, which is the key to determining the topological texture and transformation. In addition, we designed two special apertures with both fourfold and sixfold symmetry properties, which were used to realize the transformation between the meron lattice and the skyrmion lattice. The demonstrated topological texture generation and transformation methods enrich the content of the topological photonics and help in understanding the mechanism of topological transformation, as well as opening up new pathways for near-field optics and metrology.

## 2. Theory

### 2.1 The topology number of optical skyrmions

The topological properties of optical skyrmions are characterized by the skyrmion number, which can be expressed as [15, 26]:

$$N = \frac{1}{4\pi} \iint_{\sigma} \bar{e} \cdot \left( \frac{\partial \bar{e}}{\partial x} \times \frac{\partial \bar{e}}{\partial y} \right) dx dy \quad (1)$$

where the  $\bar{e}$  represents the real part of the unit vector of the local electric field, i.e.,

$\bar{e} = \text{Re}(E_x, E_y, E_z) / \sqrt{|E_x|^2 + |E_y|^2 + |E_z|^2}$  and  $\sigma$  denotes the region to confine the skyrmion.

For a skyrmion texture, the skyrmion number  $N$  is an integer ( $\pm 1$ ) and can be phenomenologically understood as the number of times the vectors wrap around a unit sphere [27]. For a meron texture, the skyrmion number  $N$  is a half-integer equal to  $\pm 1/2$ , representing the vectors can cover a half unit sphere.

### 2.2 The electric field skyrmion on the metal-air optical interface

The two-dimensional SPPs field is an ideal configuration to form the optical skyrmions [15]. As shown in Fig. 1, we build a simple structureless model to excite the SPPs that the electric field vectors present a skyrmion texture. The incident light is a focused left-handed circularly polarized vortex beam with a wavelength of 632.8 nm, whose spin angular momentum (SAM)  $s = 1$  and orbital angular momentum (OAM)  $l = -1$ . It illuminates on the three-layer system composed of a thin silver film sandwiched between air and glass substrate. The thickness of the silver film is 45 nm and the optical constants of silver follow the Johnson-Christy model. The refractive index of the air and glass substrate are 1 and 1.515, respectively. Lastly, an oil-immersion objective lens with a large NA has been used to satisfy the wave vector matching condition.

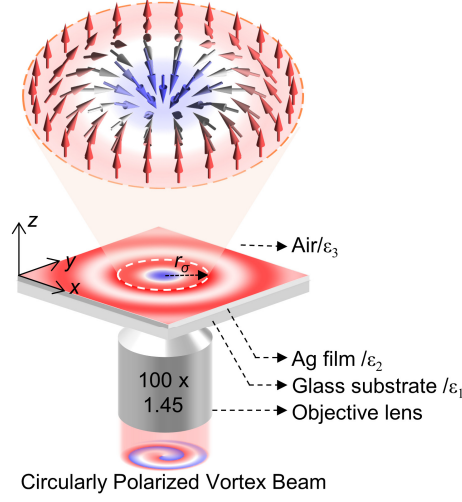


Fig. 1. Schematic diagram for the generation of the electric Néel-type skyrmion.

Following the Richard-Wolf vector diffraction theory [28, 29], the electric field of the SPPs excited on the metal-air optical interface can be derived as:

$$\begin{aligned} E_r &= E_{r1} + E_{r2} \\ E_\varphi &= E_{\varphi1} + E_{\varphi2} \\ E_z &= E_{z1} \end{aligned} \quad (2)$$

where

$$\begin{aligned} E_{r1} &= \frac{\pi}{\lambda} \cdot i^m \cdot \exp(im\phi_s) \int_0^\alpha \sqrt{(\cos\theta_1)} \cdot l_0(\theta_1) \cdot \exp(ik_2 \cos\theta_2(z+z_0)) \cdot \exp(-ik_1 z_0 \cos\theta_1) \\ &\quad \cdot \sin\theta_1 \cdot t_p^r(\theta_1) \cdot \cos\theta_2 \cdot [J_{m+1}(k_1 r \sin\theta_1) - J_{m-1}(k_1 r \sin\theta_1)] d\theta_1 \end{aligned} \quad (3)$$

$$\begin{aligned} E_{r2} &= -\frac{\pi}{\lambda} \cdot i^m \cdot \exp(im\phi_s) \int_0^\alpha \sqrt{(\cos\theta_1)} \cdot l_0(\theta_1) \cdot \exp(ik_2 \cos\theta_2(z+z_0)) \cdot \exp(-ik_1 z_0 \cos\theta_1) \\ &\quad \cdot \sin\theta_1 \cdot t_s(\theta_1) \cdot [J_{m+1}(k_1 r \sin\theta_1) + J_{m-1}(k_1 r \sin\theta_1)] d\theta_1 \end{aligned} \quad (4)$$

$$\begin{aligned} E_{\varphi1} &= \frac{\pi}{\lambda} \cdot i^{m-1} \cdot \exp(im\phi_s) \int_0^\alpha \sqrt{(\cos\theta_1)} \cdot l_0(\theta_1) \cdot \exp(ik_2 \cos\theta_2(z+z_0)) \cdot \exp(-ik_1 z_0 \cos\theta_1) \\ &\quad \cdot \sin\theta_1 \cdot t_p^r(\theta_1) \cdot \cos\theta_2 \cdot [J_{m+1}(k_1 r \sin\theta_1) + J_{m-1}(k_1 r \sin\theta_1)] d\theta_1 \end{aligned} \quad (5)$$

$$\begin{aligned} E_{\varphi2} &= \frac{\pi}{\lambda} \cdot i^{m-1} \cdot \exp(im\phi_s) \int_0^\alpha \sqrt{(\cos\theta_1)} \cdot l_0(\theta_1) \cdot \exp(ik_2 \cos\theta_2(z+z_0)) \cdot \exp(-ik_1 z_0 \cos\theta_1) \\ &\quad \cdot \sin\theta_1 \cdot t_s(\theta_1) \cdot [J_{m+1}(k_1 r \sin\theta_1) - J_{m-1}(k_1 r \sin\theta_1)] d\theta_1 \end{aligned} \quad (6)$$

$$\begin{aligned} E_{z1} &= \frac{2\pi}{\lambda} \cdot i^{m+1} \cdot \exp(im\phi_s) \int_0^\alpha \sqrt{(\cos\theta_1)} \cdot l_0(\theta_1) \cdot \exp(ik_2 \cos\theta_2(z+z_0)) \cdot \exp(-ik_1 z_0 \cos\theta_1) \\ &\quad \cdot \sin\theta_1 \cdot t_p^z(\theta_1) \cdot \sin\theta_2 \cdot J_m(k_1 r \sin\theta_1) d\theta_1 \end{aligned} \quad (7)$$

Here,  $m$  is the total angular momentum expressed as  $m = s + l$ .  $\alpha$  is the maximum allowed incident angle of the objective lens, which can be calculated through  $\alpha = \arcsin(\text{NA}/n_i)$ , and  $n_i$  is the refractive index of the medium. We assume that the electric field of the incident beam satisfies the Bessel-Gauss distribution, which can be expressed as:

$$l_0(\theta_1) = \exp\left[-\beta_0^2 \left(\frac{\sin \theta_1}{\sin \alpha}\right)^2\right] J_1\left(2\beta_0 \frac{\sin \theta_1}{\sin \alpha}\right),$$

where  $\beta_0$  is the ratio of the pupil radius and the beam waist, and  $J_m(x)$  denotes the  $m$  order Bessel function of the first kind. The  $t_p^r, t_s$  and  $t_p^z$  are the transmission efficiencies of  $E_r, E_\phi$ , and  $E_z$  components through the silver film at incident angle of  $\theta_1$ , respectively, which can be calculated through the Fresnel transmission coefficients [30].

### 3. Results

#### 3.1 The isolated electric Néel-type skyrmion

Based on the Eqs. (2)-(7), we calculate the electric field on the metal film. In addition, we build a model using Lumerical FDTD Solutions software with the same structure parameters to verify the correctness of the theory. The calculations are shown in Fig. 2(a-c). It is clear that the radial and longitudinal components  $E_r$  and  $E_z$  in cylindrical coordinates are circularly symmetric, and the azimuthal component  $E_\phi$  is almost zero, which means that the vectors will change in the longitudinal plane. At the field center,  $E_r$  is equal to zero and  $E_z$  reaches a negative peak, implying that the vector is “down” in this position. Meanwhile,  $E_z$  shows a significant increase from the center to the dotted black circle boundary, indicating that the vectors will transition from a “down” state to an “up” state. These properties will promote the vectors to evolve to a special spin texture, analogous to the hedgehog structure, namely the Néel-type skyrmion. The skyrmion number is equal to one which can be calculated through Eq. (1). We plot the cross-section of the electric field components along the x-axis in Fig. 2(d) and define the first positive peak positions of  $E_z$  as the optical skyrmion boundary, as shown by the black dotted line which ranges from -380 nm to 380 nm (pink highlighted areas). The simulations are shown in Fig. 2(e-h), which show great agreement with the calculations.

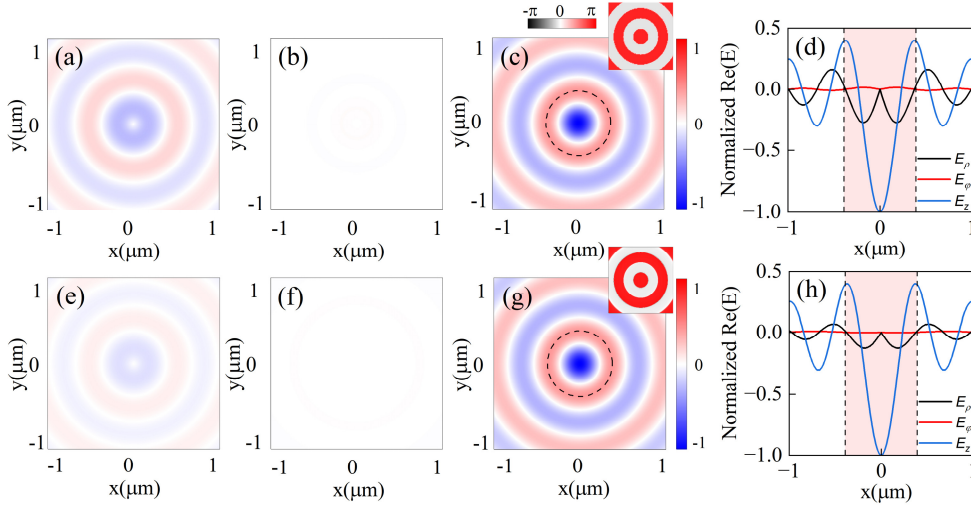


Fig. 2. The electric field components of the SPPs generated on the metal-air interface. (a-c) Theoretical electric field components for (a)  $E_r$ , (b)  $E_\phi$  and (c)  $E_z$  in cylindrical coordinates, where the inset in (c) displays the phase. (d) The normalized cross-section of the electric field components along the x-axis, the light-pink region and the black dotted lines represent the confines of the skyrmion. (e-g) The same electric field distributions from simulation.

This skyrmion texture is determined by the spin-orbit coupling and the interference of the evanescent wave. When the circularly polarized vortex beam is tightly focused, the spin-orbit coupling occurs naturally [31, 32]. The spin-to-orbital angular momentum conversion can

affect the wavefront phase, as well as the electric field distribution in the focal plane [33, 34], which provides the possibility of modulating the electric field vectors into the skyrmionic distribution. In our model, the SAM and OAM of the incident light are opposite, thus the total angular momentum  $m$  is zero. Based on Eq. (7), the spiral phase term  $\exp(im\phi_s)$  will be eliminated, resulting in a non-spiral pattern for the phase of  $E_z$ , as shown in the insets of Fig. 2(c) and (g). In addition, the curve of  $E_z$  has a Bessel distribution due to the presence of the zero-order Bessel function, which can be found in Fig. 2(d) and (h). When the circular symmetry source is focused on the optical interface, the ring-shaped SPPs are excited and propagate toward the center, resulting in a standing wave due to constructive interference. Finally, the isolated Néel-type field skyrmion is formed due to the unique distributions of the electric field components.

### 3.2 Symmetry constraints and phase control for topological transformation

In section 2.2, we have derived the analytical solution of the evanescent wave on the surface, however, it should be noted that this solution is based on the circular symmetry conditions, which is the key to generating the isolated skyrmion. In this section, we introduced a square and hexagonal aperture to constrain the symmetry of the field. Meanwhile, the initial phase of the light has been controlled, helping to transform different topological textures. The schematic diagram of this model is shown in Fig. 3(a), where the red and blue lines represent two incident lights with  $\Delta\phi$  phase difference, and the symmetry aperture is placed after the focused beam.

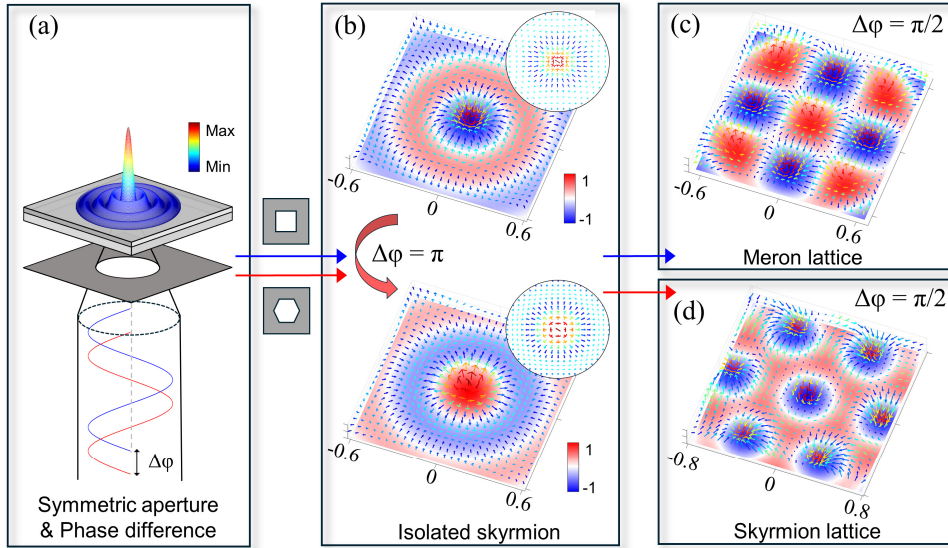


Fig. 3. Schematic diagram for the topological transformation. (a) The model for transformation, with a circle symmetric aperture under the metal-glass structure, and the intensity distribution of the evanescent field is shown on the surface. The red and blue curves represent the incident beams with  $\Delta\phi$  phase difference. (b) The electric field vector distribution with opposite skyrmion number. The background is the normalized z-component of the evanescent field. The 3D arrows indicate the directions of the electric field vectors, and the insets show the top view of it. All arrows share the same colormap with that in (a). (c-d) The meron lattice (c) and the skyrmion lattice (d) generated with a square and hexagonal aperture, respectively.

Replacing the circular aperture with a square or hexagonal aperture, the isolated skyrmions can also be generated. As shown in the top of Fig. 3(b), the background is the normalized real part of  $E_z$ . It increases from the center to the boundary, and the arrows evolve from the "down" state to the "up" state. The 3D vector distribution is consistent with a Néel-type skyrmion, whose skyrmion number is minus one. The inset is the 2D vector distribution, whose arrows point to

the center radially. We use this case as a basis for topological transformation. In this condition, we control the initial phase of the incident light with a  $\pi$  phase difference. Thus, the topological inversion is realized, as shown in the bottom of Fig. 3(b). The z-component of the evanescent field shows an opposite distribution compared with that in the top figure. It also presents the Néel-type skyrmion but the skyrmion number is one, and the 2D vectors point outward radially. Thus, we can conclude that both the circular, square, and hexagonal aperture can generate the isolated Néel-type skyrmion, and the topological inversion can be realized with a  $\pi$  phase difference.

In particular, if the phase difference is  $\pi/2$ , the transformation from the isolated skyrmion to the meron lattice or the skyrmion lattice can be realized with above apertures. For the square aperture,  $E_z$  is shown in Fig. 3(c), which has a lattice-like intensity distribution, with adjacent cells having opposite intensities. In each unit cell, it increases or decreases from the central extremum to the edge where  $E_z$  is zero. The electric field vectors tilt progressively from the central “up” or “down” state to the edge, where the direction becomes horizontal. Thus, the meron texture is formed and confined in a square cell, whose skyrmion number is equal to  $\pm 1/2$ . For the hexagonal aperture, the z-component of the electric field is shown in Fig. 3(d), which exhibits a hexagonal distribution. In each unit cell,  $E_z$  increases from the central minimum to zero and then reaches a maximum, and the vectors show the skyrmion texture, forming the skyrmion lattice. Notably, it is easy and convenient to realize the continuous change of the initial phase of light in experiments and simulations, so the continuous transformation can also be realized. Videos S1 and S2 show this continuous evolution from the isolated skyrmion to the meron lattice and the skyrmion lattice, respectively.

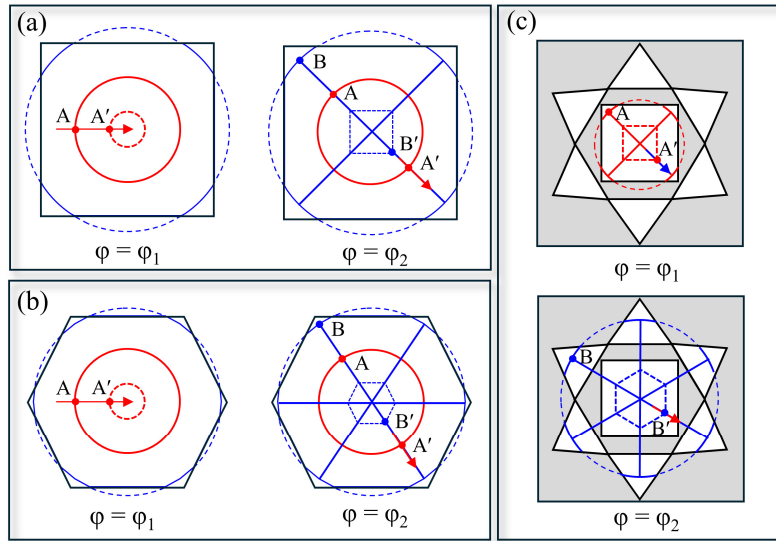


Fig. 4. The forming and transformation mechanism of the topological texture. (a-b) The apertures for transforming the isolated skyrmion to (a) the meron lattice and (b) the skyrmion lattice. (c) The composite aperture for the transformation between the meron lattice and the skyrmion lattice.

It should be noted that the symmetry of the field determines the possible presentation forms of the topological texture. The reason why the square and hexagonal apertures can realize the topological transformation is that they have double symmetry properties, i.e., circular symmetry in the center and fourfold or sixfold symmetry in the boundary (the circular symmetry condition is truncated by the boundary). As shown in Fig. 4(a), the solid red line (center) and blue line (boundary) show two different symmetries. When the initial phase  $\varphi$  is equal to  $\varphi_1$ , the circular symmetric evanescent waves (position A, red solid line) propagate radially toward the center

(position A', red dashed line), so the standing waves in the central region have circularly symmetric properties and oscillate like a wave of water, forming the isolated skyrmion. When the initial phase changes to  $\varphi_2$  and  $\Delta\varphi = \varphi_2 - \varphi_1 = \pi/2$ , the evanescent waves at the corners of the aperture (position B, blue solid line) propagate across the center and arrive at the position B'. It interferes with the waves from other corners in the central region, resulting in the standing waves exhibiting tetragonal symmetry properties and forming the meron lattice. Similar to the square aperture, the hexagon aperture also has double symmetry. As shown in Fig. 4(b), the standing waves in the central area are circularly symmetric (left, red dashed line) and hexagonal symmetric (right, blue dashed line) with the initial phase set to  $\varphi_1$  and  $\varphi_2$ , respectively. Thus, the transformation from the isolated skyrmion to the skyrmion lattice can be realized. Videos S3 and S4 show the propagation and interference of the evanescent waves. Furthermore, based on the above analysis, we designed a composite aperture that consisted of a square aperture in the central area and a sixfold aperture outside the square, as shown in Fig. 4(c). With the control of the initial phase, the symmetry of the standing wave in the center will change, resulting in the transformation between the meron and skyrmion lattices.

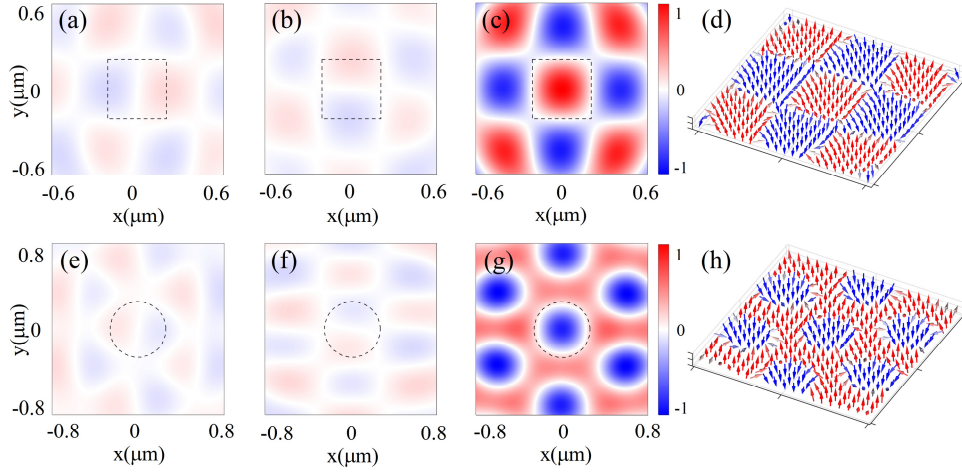


Fig. 5. The electric field components and vector distribution of the evanescent field generated by the composite aperture. (a-c) The normalized electric field components for (a)  $E_x$ , (b)  $E_y$ , and (c)  $E_z$  in cartesian coordinates, and the initial phase is  $\varphi_1$ . (d) The unit vector distribution of the evanescent field shows the meron texture. (e-h) The same distribution with that in (a-d) but the initial phase is  $\varphi_2$ .

The simulation with the composite aperture has been shown in Fig. 5. When the initial phase is  $\varphi_1$ , the meron texture appears. As shown in Fig. 5(a-b), the  $E_x$  and  $E_y$  are symmetric along the y- and x-axis in the topological domain wall marked by the black dashed line, respectively. In Fig.5(c), the  $E_z$  shows a similar distribution with that in Fig. 3(c), which presents obvious mesh-like properties. The unit field vectors have been shown in Fig.5(d). Switching the initial phase to  $\varphi_2$ , the topological texture transforms to the skyrmion lattice. As shown in Fig. 5(e-g), the  $E_x$  and  $E_y$  are also symmetric in each unit cell, and the  $E_z$  is hexagonal symmetric but with a rotation angle with respect to that in Fig. 3(d). The unit vector distribution has been shown in Fig.5(h). It should be noted that this composite aperture has triple symmetry, but it cannot realize the transformation between three different topological textures. This is because the range of the phase is limited, which cannot cover the entire aperture, especially the central circular region. In addition, the field vector transformation between the meron lattice and the skyrmion lattice has been shown in Video S5, and the interference has been shown in Video S6.

### 3.3 The optimized aperture for transformation

Although the topological transformation has been achieved with above apertures, the range of the lattice is small. In fact, the shape of the aperture that supports the transformation is not fixed but is possible as long as the double symmetry is satisfied. Therefore, we designed an optimized aperture which is used for the transformation between the meron lattice and the skyrmion lattice but with a larger range. The shape of the aperture is shown in Fig. 6(a), which shows fourfold symmetry within the red dashed line and sixfold symmetry between the red and blue dashed lines. The radius of the red dashed circle is 6  $\mu\text{m}$ , and the size of the aperture is 20  $\mu\text{m}$ . With the control of the initial phase, the meron lattice and the skyrmion lattice are formed and can transform into each other, as shown in Fig. 6(b-c). It should be noted that the phase difference between the two topological lattices is no longer  $\pi/2$  but a smaller radian equal to 1.13. In Fig. 6(d-f), we plot the electric field components of the meron lattice, whose x and y components show significant strip distribution, which is different from that in Fig. 5(a) and (b). Although the distributions are generally different, the components in each unit cell are similar, so both field vectors show the meron texture. In Fig. 6(g-i), we plot the electric field components of the skyrmion lattice, which is similar with that in Fig. 5(e-g) but with a larger range. Surprisingly, this optimized aperture is very different from the composite aperture, but they give similar results, which implies that the topological textures generated with this method are robust, as well as robust to the slight change in the shape of the aperture. The transformation and interference are shown in Videos S7 and S8, respectively.

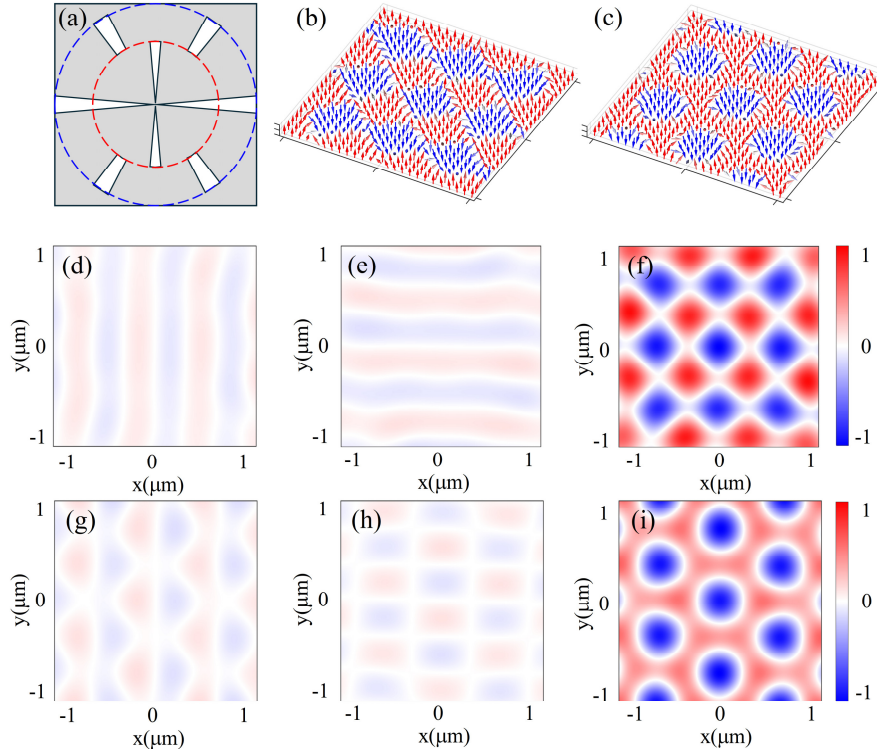


Fig. 6. The simulation with the well-designed double symmetric aperture. (a) The shape of the aperture, where the red dashed line is the dividing line between two symmetric areas. (b-c) The meron lattice (b) and the skyrmion lattice (c) based on the unit vectors of the electric field. (d-f) The normalized electric field components ( $E_x$ ,  $E_y$ , and  $E_z$ ) for the meron lattice (d-f) and the skyrmion lattice (g-i) in cartesian coordinates. The phase difference is 1.13 rad.

## 4. Discussion and conclusion

It is noteworthy that the initial phase can continuously change in our system, thus the continuous transformation can be realized, which shows great importance for observing and understanding the transformation between different topological textures. Through a well-designed multi-symmetric aperture, other complex topological transformations can be realized, even the transformation involves three or more different topological textures in the future. The described method can be extended to other wavelengths. In addition, different topological textures correspond to different initial phases, thus the highly sensitive phase sensing may be realized. Moreover, this method also provides new opportunities for the photonic spin skyrmion transformation. It should be mentioned that while this article was being written, an independent work [35] has demonstrated a fascinating transformation method between skyrmion and meron textures. They creatively generated the photonic spin textures on the metallic meta-surface that has a well-designed structural period, and tuned the textures with different wavelengths, which is distinct from our work based on the double symmetry and phase control.

In summary, we build a simple model for generating the isolated skyrmion and derive the analytical solution of the evanescent field on the metal surface. By introducing a series of apertures with multi-symmetry properties, the transformations between the isolated skyrmion, the meron lattice, and the skyrmion lattice are realized. We analyze the mechanism of the transformation, demonstrating that the symmetry of the field determines the possible forms of the topological textures, and the initial phase determines the actual presentation form of them. Our investigation realizes for the first time the continuous topological transformation between the field skyrmion and meron topology in the optical field. The double symmetry and phase control increase the freedom of optical field manipulation, as well as open up a new avenue for the subsequent investigations in metrology and topological photonics.

## References

1. T. H. R. Skyrme, "A unified field theory of mesons and baryons," *Nuclear Physics* **31**, 556-569 (1962).
2. D. C. Wright and N. D. Mermin, "Crystalline liquids: the blue phases," *Reviews of Modern Physics* **61**, 385-432 (1989).
3. T.-L. Ho, "Spinor Bose Condensates in Optical Traps," *Physical Review Letters* **81**, 742-745 (1998).
4. S. Mühlbauer, et al., "Skyrmion lattice in a chiral magnet," *Science (New York, N.Y.)* **323**, 915 - 919 (2009).
5. K. Moon, et al., "Spontaneous interlayer coherence in double-layer quantum hall systems: Charged vortices and kosterlitz-thouless phase transitions," *Physical Review B* **51**, 5138-5170 (1995).
6. X. Z. Yu, et al., "Transformation between meron and skyrmion topological spin textures in a chiral magnet," *Nature* **564**, 95-98 (2018).
7. A. Fert, et al., "Skyrmions on the track," *Nature Nanotechnology* **8**, 152-156 (2013).
8. S. S. P. Parkin, et al., "Magnetic Domain-Wall Racetrack Memory," *Science* **320**, 190-194 (2008).
9. J. Iwasaki, et al., "Current-induced skyrmion dynamics in constricted geometries," *Nature Nanotechnology* **8**, 742-747 (2013).
10. X. Zhang, et al., "Magnetic skyrmion logic gates: conversion, duplication and merging of skyrmions," *Scientific Reports* **5**, 9400 (2015).
11. X. Zhang, et al., "Magnetic skyrmion transistor: skyrmion motion in a voltage-gated nanotrack," *Scientific Reports* **5**, 11369 (2015).
12. Y. Shen, et al., "Generation of optical skyrmions with tunable topological textures," *ACS Photonics* **9**, 296-303 (2022).
13. A. Yang, et al., "Spin - Manipulated Photonic Skyrmion - Pair for Pico - Metric Displacement Sensing," *Advanced Science* **10**, 2205249 (2023).
14. Y. Shen, et al., "Optical skyrmions and other topological quasiparticles of light," *Nature Photonics* **18**, 15-25 (2024).
15. S. Tsesses, et al., "Optical skyrmion lattice in evanescent electromagnetic fields," *Science* **361**, 993-996 (2018).
16. S. Tsesses, et al., "Spin-Orbit Interaction of Light in Plasmonic Lattices," *Nano Letters* **19**, 4010-4016 (2019).
17. T. J. Davis, et al., "Ultrafast vector imaging of plasmonic skyrmion dynamics with deep subwavelength resolution," *Science* **368**, eaba6415 (2020).
18. Q. Zhang, et al., "Exploring optical resonances of nanoparticles excited by optical skyrmion lattices," *Optics Express* **27**, 7009 (2019).
19. C. Bai, et al., "Dynamic tailoring of an optical skyrmion lattice in surface plasmon polaritons," *Optics Express* **28**, 10320 (2020).
20. Z.-L. Deng, et al., "Observation of localized magnetic plasmon skyrmions," *Nature Communications* **13**, 8 (2022).

21. L. Du, et al., "Deep-subwavelength features of photonic skyrmions in a confined electromagnetic field with orbital angular momentum," *Nature Physics* **15**, 650-654 (2019).
22. X. Lei, et al., "Photonic spin lattices: Symmetry constraints for skyrmion and meron topologies," *Physical Review Letters* **127**, 237403 (2021).
23. Q. Zhang, et al., "Bloch-type photonic skyrmions in optical chiral multilayers," *Physical Review Research* **3**, 023109 (2021).
24. Q. Zhang, et al., "Optical topological lattices of Bloch-type skyrmion and meron topologies," *Photonics Research* **10**, 947 (2022).
25. M. Lin, et al., "Photonic Spin Skyrmion with Dynamic Position Control," *ACS Photonics* **8**, 2567-2572 (2021).
26. N. Nagaosa and Y. Tokura, "Topological properties and dynamics of magnetic skyrmions," *Nature Nanotechnology* **8**, 899-911 (2013).
27. J. P. Liu, et al., *Skyrmions: Topological Structures, Properties, and Applications* (CRC Press, 2016), p. 502.
28. E. Wolf, "Electromagnetic diffraction in optical systems - I. an integral representation of the image field," *Proceedings of the Royal Society of London. Series A. Mathematical and Physical Sciences* **253**, 349-357 (1959).
29. B. Richards, et al., "Electromagnetic diffraction in optical systems, II. structure of the image field in an aplanatic system," *Proceedings of the Royal Society of London. Series A. Mathematical and Physical Sciences* **253**, 358-379 (1997).
30. Z. Man, et al., "Dynamic plasmonic beam shaping by vector beams with arbitrary locally linear polarization states," *Applied Physics Letters* **105**, 011110 (2014).
31. K. Y. Bliokh, et al., "Spin-orbit interactions of light," *Nature Photonics* **9**, 796-808 (2015).
32. J. S. Eismann, et al., "Spin-orbit coupling affecting the evolution of transverse spin," *Physical Review Research* **1**, 033143 (2019).
33. Y. Zhao, et al., "Spin-to-Orbital Angular Momentum Conversion in a Strongly Focused Optical Beam," *Physical Review Letters* **99**, 073901 (2007).
34. S. Tsesses, et al., "Spin-Orbit Interaction of Light in Plasmonic Lattices," *Nano Letters* **19**, 4010-4016 (2019).
35. M. Lin, et al., "Wavelength-tuned transformation between photonic skyrmion and meron spin textures," *Applied Physics Reviews* **11**(2024).